Western Indian Ocean
JOURNAL OF
Marine Science

Special Issue 1/2020 | Dec 2020 | ISSN: 0856-860X

Productivity in the East African Coastal Current under Climate Change

Guest Editors | Francis Marsac and Bernadine Everett

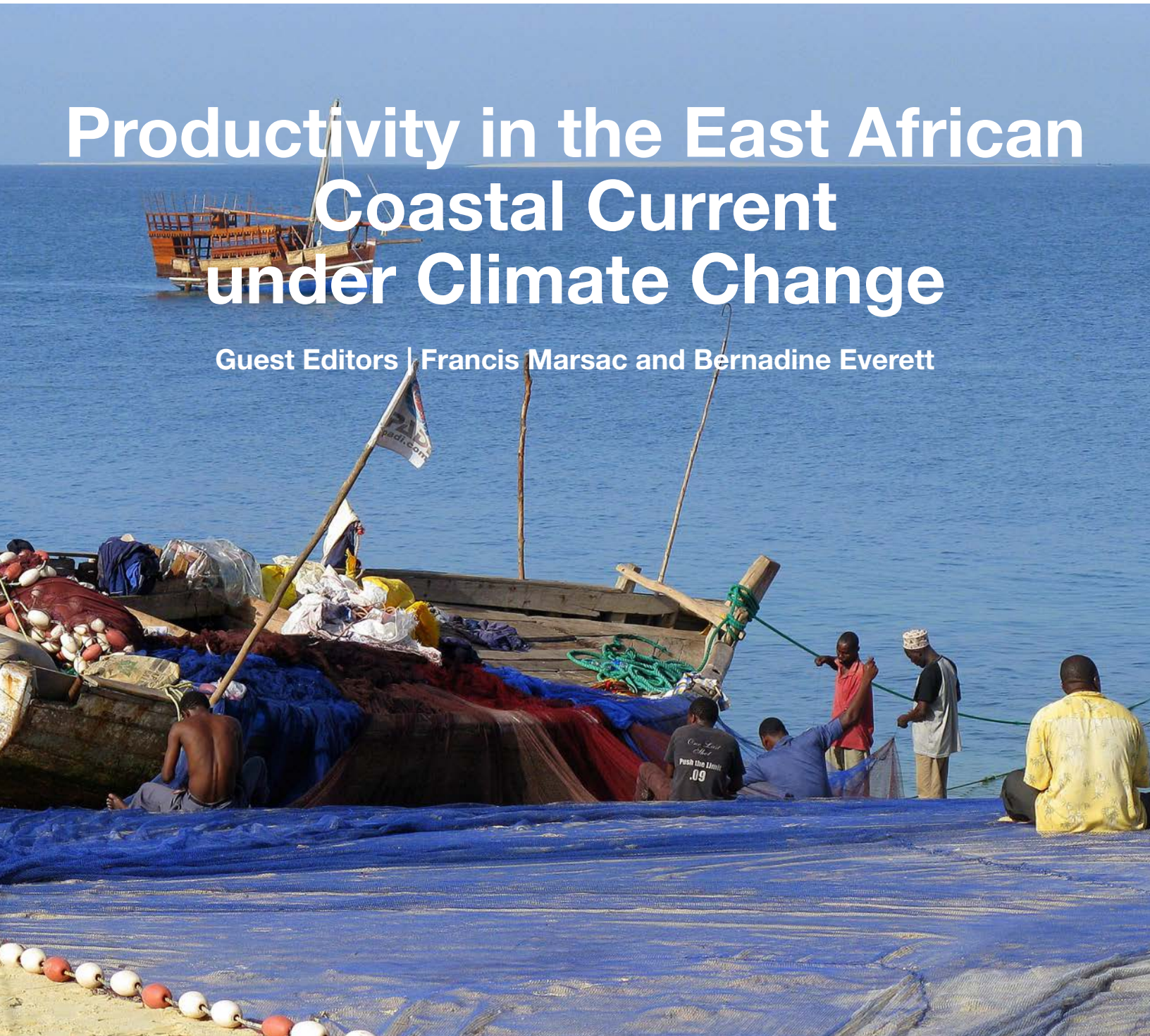

Western Indian Ocean
JOURNAL OF
Marine Science

Published biannually

Aims and scope: The *Western Indian Ocean Journal of Marine Science* provides an avenue for the wide dissemination of high quality research generated in the Western Indian Ocean (WIO) region, in particular on the sustainable use of coastal and marine resources. This is central to the goal of supporting and promoting sustainable coastal development in the region, as well as contributing to the global base of marine science. The journal publishes original research articles dealing with all aspects of marine science and coastal management. Topics include, but are not limited to: theoretical studies, oceanography, marine biology and ecology, fisheries, recovery and restoration processes, legal and institutional frameworks, and interactions/relationships between humans and the coastal and marine environment. In addition, *Western Indian Ocean Journal of Marine Science* features state-of-the-art review articles and short communications. The journal will, from time to time, consist of special issues on major events or important thematic issues. Submitted articles are subjected to standard peer-review prior to publication.

Manuscript submissions should be preferably made via the African Journals Online (AJOL) submission platform (http://www.ajol.info/index.php/wiojms/about/submissions). Any queries and further editorial correspondence should be sent by e-mail to the Chief Editor, wiojms@fc.ul.pt. Details concerning the preparation and submission of articles can be found in each issue and at http://www.wiomsa.org/wio-journal-of-marine-science/ and AJOL site.

Disclaimer: Statements in the Journal reflect the views of the authors, and not necessarily those of WIOMSA, the editors or publisher.

ISSN 0856-860X

Cover image: Stonetown, Zanzibar (© Bernadine Everett, 2012)

Biophysical modelling of coastal upwelling variability and circulation along the Tanzanian and Kenyan coasts

Issufo Halo[1,2,6]*, Philip Sagero[3], Majuto Manyilizu[4], Shigalla B. Mahongo[5,6,7]

[1] Conservation and Marine Sciences, Cape Peninsula University of Technology, P.O. Box 652, Cape Town, 8000, South Africa

[2] Nansen-Tutu Centre for Marine Environmental Research, Private Bag X3, 7700 Cape Town, South Africa

[3] Kenya Meteorological Department, PO Box 30259-00100, Nairobi, Kenya

[4] College of Informatics and Virtual Education, University of Dodoma, PO Box 490, Dodoma, Tanzania

[5] Tanzania Fisheries Research Institute, PO Box 9750, Dar es Salaam, Tanzania

[6] Center for Sustainable Oceans, Cape Peninsula University of Technology, P.O. Box 652, Cape Town, 8000, South Africa

[7] Lake Victoria Fisheries Organization, P.O. Box 1625, Jinja, Uganda.

* Corresponding author: haloi@cput.ac.za

Abstract

Ocean circulation, upwelling phenomena and chlorophyll-*a* concentrations were investigated within the framework of numerical model simulations with 1/12° nested horizontal grid-size, in the tropical western Indian Ocean, along the coasts of Tanzania and Kenya. Ekman driven upwelling exhibited high levels of spatial and temporal variability in the region, characterized by a more vigorous occurrence/intensification during the Northeast than the Southwest Monsoon season. A similar trend was observed for chlorophyll-*a* distribution, but with an additional strong contribution during the inter-monsoon period from March to April. Trend analysis of a SST-derived coastal upwelling index (CUI) computed over the Pemba Channel and offshore of the East African Coastal Current (EACC), for 24 years (1990 - 2013), revealed a general linear relation of the form CUI(yr) = 2.4×10^{-7}yr − 285, with a steady small annual increase of the upwelling phenomena by 0.0024/year ≃ 4% during the whole period of the simulation, which could be attributed to documented increasing trends of wind intensity and water volume transport in the region. The CUI exhibited the two most dominant peaks of variabilities on the range of annual and semi-annual timescales. The wind-stress southward component and the easting/westing veering of the northward EACC at 6°S revealed that these parameters were moderate and significantly correlated with the CUI ($r = -0.53$ and 0.52, $p<0.05$) respectively, further suggesting its intensification during the Northeast Monsoon season.

Keywords: Ekman pumping and suction, Wind stress curl, Upwelling and downwelling, Ocean models

Introduction

Coastal upwelling events have been the subject of high interest among physical and biological oceanographers for many decades (Brink *et al*., 1983; Bakun, 1998; Durand *et al*., 1998; Capet *et al*., 2004; Echevin *et al*., 2005). Understandably, coastal upwellings are among the most productive marine eco-systems, providing food, sustaining fisheries and other economic and ecological services of great importance to human society (Cury and Roy, 1989; Bakun, 1998; Lett *et al*., 2007; Garcia-Reyes *et al*., 2015).

As a result of the on-going global concerns about climate change (Garcia-Reyes and Mahongo (this issue)) and associated perturbations on the patterns of general atmospheric and oceanic circulations, many scientific studies have directed their attention towards understanding how such changes may impact the strength/intensity of upwelling systems around the world (Garcia-Reyes *et al*., 2015). Only recently have these concerns been raised in the western Indian Ocean and awareness among the marine scientific community and relevant stakeholders has been raised (Roberts, 2015).

http://dx.doi.org/10.4314/wiojms.si2020.1.5

Along the coasts of Tanzania and Kenya the development of a near-shore negative wind-stress curl, and consequent positive Ekman vertical velocities (i.e. Ekman suction) during the Northeast Monsoon as observed by Collins *et al*. (2012) and Manyilizu *et al*. (2016), suggest the occurrence of an active upwelling phenomenon. The opposite is also observed during the Southwest Monsoon (Collins *et al*., 2012), leading to a downwelling phenomenon (i.e. Ekman pumping). Coastal upwelling along the Tanzanian and Kenyan continental shelves can be visually diagnosed from thermal expressions of high resolution sea surface temperature (SST) products (able to resolve detailed patterns of spatial and temporal scale variabilities, for example fronts, (SST gradients), and filaments as depicted in Fig. 1) simulated by the Regional Ocean Modelling Systems (ROMS) with a horizontal grid-resolution of 1/12°, for the 2nd January of year 8. In Fig. 1, the super-imposed vectors indicate the direction of the flow field (circulation). The snapshot portrays a typical situation prevalent in the region, characterized by the presence of the warmer EACC, that permanently propagates northward along the Tanzanian and Kenyan coasts (Swallow *et al*., 1991; Nyandwi, 2013). The EACC receives most of its water supply from the warmer South Equatorial Current (SEC), after its splitting on arrival at the African coast near 12°S (Swallow *et al*., 1991; Schott *et al*., 1988, 2009; Manyilizu *et al*., 2016). Upon receiving such supply, the EACC becomes a well-defined and distinct structure along the coasts of Tanzania and Kenya between 11°S and 3°S, and it carries about 19.9 Sv (1 Sv = 10^6 m^3s^{-1}) of the volume transport in the upper 300 m of the water column, across a zonal distance of 120 km offshore (Swallow *et al*., 1991). Its main core lies at the offshore side of the chain of islands formed by Mafia, and Unguja and Pemba (Zanzibar archipelago), whereby parts of the flow upslopes onto the narrow continental shelf and recirculates around the islands, as documented by Mahongo and Shaghude (2014), Roberts (2015), and Mayorga-Adame *et al*. (2016).

The major gateway for the upsloping flow appears to be located between Unguja and Pemba Islands, as observed and captured by the hydrographic measurements presented by Nyandwi (2013), Roberts (2015) and the modelling study by Mahongo and Shaghude (2014). For details of the main current systems in the western Indian Ocean (WIO), the reader is referred to the works by Schott *et al*. (2009), especially the model data comparison section (see Fig. 2).

A paucity of hydrographic data in this region exists with few dedicated studies to investigate the nature and characteristics of the East African upwelling events along the coasts of Tanzania and Kenya even though these localized upwelling events help to service the need (subsistence) of the local coastal communities which heavily depend on artisanal fishing (Mapunda,1983; Ministry of Agriculture Livestock and Fisheries, 2016). It is only recently that regional initiatives to study these upwelling events in the WIO region along these coasts have emerged, within the framework of the second International Indian Ocean Expedition (IIOE-2), through the Western Indian Ocean Upwelling Research Initiative (WIOURI) project (Roberts, 2015), and the Productivity of the East African Coastal Current (PEACC) project (between 2016-2018), endorsed by the IIOE-2, and supported through a MASMA grant from the Western Indian Ocean Marine Science Association (WIOMSA) (https : //www.wiomsa.org/ongoing – project/), from which the present study is derived.

Disturbing environmental climate change patterns have been recently diagnosed in the WIO equatorial region, reflected in the form of (1) excessive unprecedented sea-surface warming (Roxy *et al*., 2014), and (2) increasing trends and intensification of the wind system and oceanic surface currents, and their kinetic energy (Mahongo *et al*., 2012; Backeberg *et al*., 2012). In this study it is therefore aimed to investigate the nature, spatial and temporal variabilities of the coastal upwelling events along the coasts of Tanzania and Kenya. The main research question is 'how do the upwelling events along the coasts of Tanzania and Kenya relate to the on-going changes of patterns in atmospheric and oceanic circulations, as documented by Mahongo *et al*., 2012 and Garcia-Reyes *et al*. [this issue].

To achieve the goal/objectives of this study, a SST's coastal upwelling index (CUI) from a high-resolution hydrodynamic model output was computed and investigated. Furthermore, the CUI variability against atmospheric winds was inspected, together with the structure of the EACC, translated in terms of its zonal and meridional velocity components.

Material and methods

Physical model

ROMS is a split-explicit free-surface ocean circulation model designed especially for accurate simulation of regional oceanic systems and coastal margins, using higher-order numerical schemes (Shchepetkin and McWilliams, 2005). The model solves the discrete

set of primitive equations of motion in a staggered C-grid, under an earth rotating reference frame using the hydrostatic and Boussinesq approximations. For details of the model kernel, it is recommended that the reader consult the paper by Shchepetkin and McWilliams (2005).

Biophysical model

The biophysical model used in this study is the medium complex level biogeochemistry NPZD model (Gruber *et al*., 2006). It simulates the simple interaction of four ecosystem properties, namely, nutrients (N), phytoplankton (P), zooplankton (Z) and detritus (D) (Fasham *et al*., 1990). To ensure a more realistic solution within the region of interest, the closing terms for phytoplankton and zooplankton used were derived from higher-order numerics instead of the usual linear schemes. For details of the model it is recommended that the reader consult the work of Fasham *et al*. (1990).

Modelling strategy

The model configuration was built using ROMSTOOLS (Penven *et al*., 2008). It consists of two-level rectangular grids, connected via a two-way nesting approach (Debreu *et al*., 2012). The outer domain ("parent model") spans from 35°E to 90°E, and 30°S to 30°N, which essentially covers the whole WIO, with a horizontal grid resolution of 1/4°, nearly 25 km. The inner domain ("child model", 38.5°E – 42°E, 10°S – 4°S) was set to cover the whole excursion of the EACC, and it runs with a horizontal grid resolution of 1/12°, about 8 km. On the vertical the configuration has been set with 60 vertical σ-layers, and the grid controlling parameters at sea-floor was θ_b=0, at sea-surface θ_s=6, and the layers thickness h_c=10.

Two different experiments were performed. The first was driven by climatological surface forcing and lateral open boundary conditions. It used monthly averages surface fields, which includes the wind-stress, fresh-water fluxes, heat-flux and salt-flux, gridded at 1/2°×1/2° derived from COADS05 (Da Silva *et al*., 1994). To boost the air-sea interaction over the COADS05 product, the surface heat-flux was augmented using a 9-km satellite derived SST (pathfinder product), as a restoring term for the boundary layer processes with a timescale of about 60 days (Colas *et al*., 2012). To augment COADS05 wind-stress (important for accurate representation of coastal dynamics), winds derived from QuikScat satellite Scatterometer Climatology of Ocean Winds (SCOW) from (1999 - 2009), gridded at 1/4°×1/4° by Risien and Chelton (2008) was used. This augmentation boosts the low resolution COADS product. For further details on boosting of the model surface forcing, consult the work by Colas *et al*. (2012). SCOW is known to capture small-scale features that are dynamically important to both the ocean and the atmosphere (e.g. SST gradient), but are not resolved in other observationally-based wind atlases or in NCEP-NCAR re-analysis fields (Risien and Chelton, 2008). The lateral open boundary fields were derived from hydrographic datasets from the World Ocean Atlas 2009 (WOA09, Conkright *et al*., 2002), gridded monthly climatology at 1° (Conkright *et al*., 2002). The flow field was derived from Ekman and geostrophic equations, the latter computed from hydrography, with the reference depth for integration set to 1000 m below the sea surface.

The second experiment was configured to account for the inter-annual variabilities. It was forced at sea-surface by wind-stress derived from the ERA Interim re-analysis product, interpolated online onto the grid, using the bulk formulation, while employing the relative-wind approach, to ensure realistic representation of kinematic energies. The lateral open boundary conditions were derived from GLORYS global re-analysis (https://www.mercator-ocean.fr/sciences-publications/glorys/). The simulations were carried out over the period spanning 1990 to 2013 with 3 years of adjustment.

The biogeochemical model was coupled to the climatology physical model through the advection-diffusion equation, whereby the state variables of the NPZD model holds a separate equation which describes its motion in time and space (Peter, 2002). The monthly climatologies for nitrate, phosphate, silicate and oxygen concentrations for the lateral open boundaries were derived from CARS2009 dataset (Ridgway *et al*., 2002). SeaWifs was used to obtain a climatology of surface chlorophyll-a concentration (WOA, 2001, Conkright *et al*., 2002). Freshwater river runoff was derived from the global climatology dataset of Dai *et al*. (2009).

CNES-CLS13 data

The large-scale oceanic surface geostrophic circulation in the region was derived from the mean dynamic topography product (CNES-CLS-13, https: //www.aviso.altimetry.fr/en//data/products/auxiliary−products/references.html). The product is computed from long-term (1993-2012) in-situ oceanographic datasets, including drifter velocities, hydrological profiles for the upper 350 m below the sea-surface, mapped

within a grid box-size of 1/4°× 1/4°. It also includes remotely sensed altimetry measurements and outputs from numerical models. The computation uses advanced processing techniques, based on multivariate objective analysis. The product is known to capture oceanographic features with relatively short scale structures, leading to better representation of the flow field when compared against previous global mean dynamic topography products (Rio and Hernandez, 2004; Rio *et al*., 2011).

Tide-gauge data

The sea-level data used to evaluate the model performance was downloaded from the Joint Achieve for Sea-Level (http://uhslc.soest.hawaii.edu/), retrieved from a single tide-gauge station deployed at reference station 151A located at the coastal island of Zanzibar, at 39.19°E, 6.15°S. While the data are provided from the source as hourly values or more frequent intervals of about 15 minutes, which are then reduced to hourly intervals, a daily time-scale from 1984 to 2018 has been used in this study. The data is calibrated, quality controlled, and made available for research purposes in a standardized format (Caldwell *et al*., 2015).

Satellite ocean colour data

To evaluate the performance of the biological component of the model, the simulated chlorophyll-a concentration against monthly mean climatology maps of sea surface chlorophyll-a concentration derived from the satellite based optical sensors MODIS-AQUA was compared. MODIS is a Moderate Resolution Imaging Spectroradiometer instrument onboard a NASA satellite (https://oceancolor.gsfc.nasa.gov). MODIS data is available from July 2002 to the present. The product used here, termed GMIS-MODIS-AQUA was extracted from the European Union Data Portal (https://data.europa.eu/data/dataset), made freely available by the European Commission Joint Research Centre. The product is gridded globally, in a logarithmic scale over a mesh of 9 km grid size. The temporal coverage ranges between 4 July 2002 and 25 January 2018.

Data Analysis and techniques

Matrix Laboratory software (MatLab, https://www.mathworks.com/) was used for the data processing, computation, and visualization. Several techniques have been implemented to extract necessary information from the datasets used in the present study. Some of these techniques were: (1) Geostrophic balance, which is a regime attained from the horizontal components of the momentum equation, when the pressure gradient force is balanced by the Coriolis force, due to the rotation of the earth. From these the geostrophic velocities of the circulation are computed as follows:

$$u = -\frac{g}{f}.\frac{\partial \eta}{\partial y} \text{ and } v = \frac{g}{f}.\frac{\partial \eta}{\partial x} \quad (1)$$

Here g and $f = 2\pi\Omega.\sin(\theta)$ represent the acceleration due to gravity and the Coriolis parameter respectively. $\Omega = \frac{2\pi}{T}$ is the frequency of the earth's rotation, with period T of about 24 hours, and θ is the latitudinal position; (2) In addition, the Multi-Tapper Method was used to compute the power-spectral density of the EACC volume transport, and the wavelet spectral analysis was applied on the CUI time series. Important references for these techniques can be found in Thomson (1982) and Smith-Boughner and Constable (2012). Freely available Toolkits for various computer operative systems can be accessed at (https://dept.atmos.ucla.edu/tcd/multi-taper-method-mtm); (3) Simple linear regression analysis was performed to inspect the trends in the CUI time series, and the Pearson's correlation coefficients were determined between CUI and geophysical parameters such as wind-stress and current velocity. Spatial distribution of areas of upwelling were mapped using Ekman suction, using the equation below:

$$U = \frac{\tau}{\rho o f Lu} \quad (2)$$

Where τ is the alongshore windstress, ρo - is the mean seawater density, f - is the Coriolis parameter (already defined earlier). Lu - is the cross-shore horizontal scale. Temporal variability of the CUI was determined based on thermal expressions of SST, following the method developed by Demarcq and Faure (2000), and adapted by Ramanantsoa *et al*. (2018) for the southern Madagascar upwelling, defined by the following equation:

$$CUI = \frac{SSToffshore - SSTinshore}{SSToffshore - SSTmean} \quad (3)$$

Where SSToffshore and SSTinshore are the computed SST average within the offshore and inshore boxes respectively shown in Fig. 1. SSTmean is the mean between the average SSToffshore and SSTinshore.

It is important to mention that the terms used in this study to qualify the statistics (i.e. the strength of the correlation coefficients and coefficients of determination) are based on the criteria adopted in the paper by Assuero *et al*. (2006).

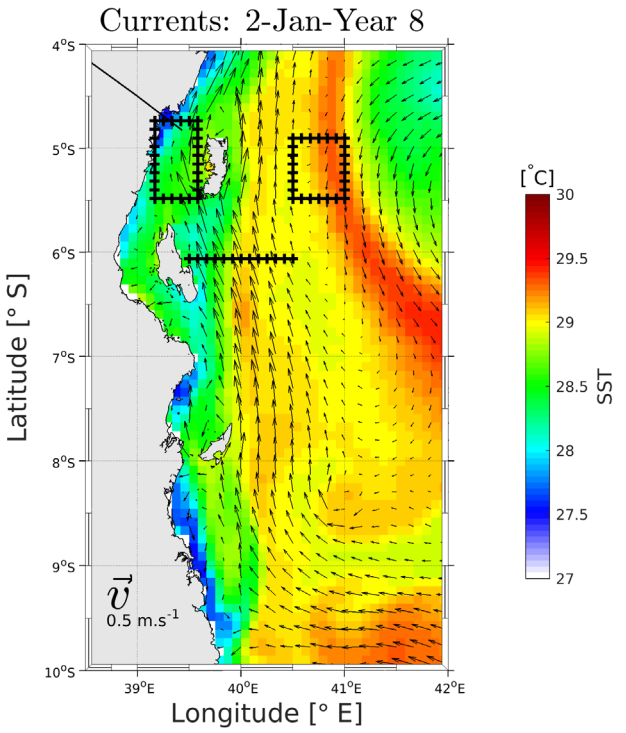

Figure 1. Model simulation of the instantaneous view of the flow field illustrating important synoptic features of the circulation (arrows), and spatial variations of the sea surface temperature (colour shading) along the coasts of Tanzania and Kenya. Output from the nested model with a horizontal grid resolution of 1/12°, for the 2nd January Year 8. The arrows indicate the flow direction. Note the boxes to the west (inshore) and to the east (offshore) of the northernmost island (Pemba), used to compute the SST upwelling index. Note also the transect at 6°S between the middle island and offshore, across the EACC, used to compute the time-series of the volume transport of the EACC shown in Figure 3. The plain line in the upper left corner of the figure, over the continent, represents the geographical border between Tanzania and Kenya.

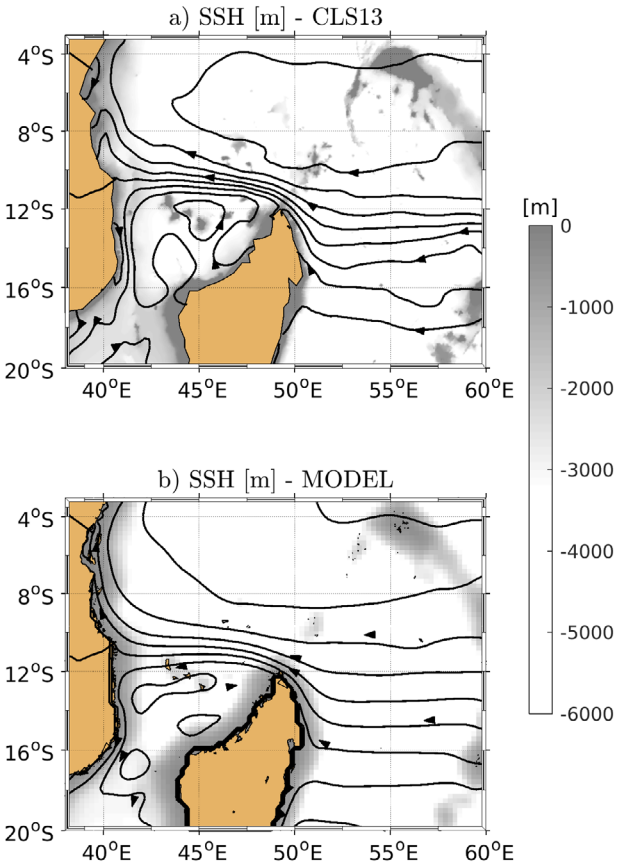

Figure 2. Model and data comparison for the large-scale oceanic geostrophic circulation, computed from variations of the sea-surface. a) Streamlines of mean dynamic topography from CLS-CNES13, and b) model simulated mean sea-surface height. Contour interval 0.05 m, and the arrows indicate the direction of the currents. Note that it reflects the circulation patterns well. Background shading shows the sea-floor topography.

Model performance

The ability of ROMS to accurately simulate the flow field in the region of interest has been demonstrated successfully in previous studies (Manyilizu *et al.*, 2014, 2016; Gamoio *et al.*, 2017), including Manyilizu *et al.* [this issue].

Large-scale circulation

To corroborate this fact, Fig. 2 shows the sea surface height (SSH) streamlines from both observations (Fig. 2a) and the result from the climatological model simulation (Fig. 2b), illustrating the upper ocean large-scale geostrophic circulation derived from variation of the sea-surface (ζ), expressed by the velocity components *(u)* and *(v)* with relation to *(x)* and *(y)* direction respectively (Equation 1).

Fig. 2a was constructed using the CNES-CLS-13 mean dynamic topography, and Fig. 2b, model climatology of sea-surface height. The contour interval is 0.05 m, the stream-arrows indicate the direction of the ocean currents, and the background shading is the seafloor topography. The model resembles the observed patterns well, characterized by the presence of the main oceanographic features of the circulation documented in many publications (Manyilizu *et al.*, 2014; Schott *et al.*, 2009). For example, a good representation of the split of the South Equatorial Current (SEC) at northeast coast of Madagascar between 16 - 17°S (Fig. 2b) is clearly seen. The impact of the mesoscale eddies in the general circulation patterns within the Mozambique Channel (as indicated by the clockwise and anticlockwise features, denoting cyclonic and anticyclonic eddies) is also clearly seen. The splitting of the western extension of the North East Madagascar Current (NEMC) at about 12°S near the African mainland into two opposing branches is also evident. The northward branch feeds the EACC along the coast of Tanzania and Kenya. The model is also able to reproduce the cross-equatorial cell, portrayed by the clockwise cyclonic recirculation

to the north of Madagascar, at the northern sector of the South Equatorial Current (SEC). This cross-equatorial cell ranges between 5 - 10°S, and is driven by Ekman pumping, in response to wind forcing at the northern boundary of the south-easterlies (Schott *et al*., 2009).

In spite of the model's ability to mimic observations well, there are also some discrepancies between them. For example, the stream-lines at the eastern boundary of the domain presented in Fig. 2 shows relatively larger spacing between the contours in the model (Fig. 2b) than in the observation (Fig. 2a). This indicates that the SEC in the model is weaker than in the observation. The reader may find it informative to compare these details (Fig. 2) with the description presented by Schott *et al*. (2009).

EACC volume transport at 6°S

To assess the ability of the model to reproduce the structure of the EACC through the water column, the volume transport of the EACC in the upper 500 m of the water column at 6°S, across the width of the current between 39.5 and 40.5°E, has been computed (Fig. 3). For reference, see the transect position in Fig. 1, which seems to capture the full structure of the current's main core. The model shows high level of transport variability, minimum and maximum fluctuations ranging between 5 and 28 Sv, observed in 1990 and 1999 respectively (Fig. 3a). The power-spectrum presented in Fig. 3b suggests dominant modes of variability (i.e. power-density which is equal or above 1 Sv^2 $year^{-1}$) ranging from intra-seasonal to inter-annual and longer time-scales (i.e. 3 - 5 years' cycle, 1 and 2 cycles $year^{-1}$ in Fig. 3b). This is consistent with the literature which indicates that these modes of variability are strongly coupled by marked seasonality (Schott *et al*., 2009; Manyilizu *et al*., 2016). The quantified annual mean was 16.2 Sv and the standard deviation was 3 Sv. Using direct hydrographic observations, Swallow *et al*. (1991) has given an estimate of 19.9 Sv. Therefore, the model results from this study show good agreement with observed data.

Sea level in Zanzibar

In order to inspect the performance of the inter-annual model experiment, the time-series variations of the sea-surface height, and its corresponding power-spectra for the entire model period, spanning from 1990 to 2013, were computed to compare against the long-term observation of sea-level from 1984 to 2018. This dataset represents the only observational data available, collected in Zanzibar by the University of Hawaii Sea-level Center (UHSLC), using a tide-gauge located at 39.19°E, 6.15°S.

As can be seen from the results presented in Fig. 4, both the model and observations show similar general patterns characterized by a consistent decreasing profile of the sea-level height prior to the year 2000, and an increasing profile after 2000. Furthermore, both products (model and observation) also capture the peak of sea-level height that occurred between 1997 and 1998, likely associated with one of the most intense historical ENSO event that severely devastated the WIO region (Schott *et al*., 2009). Good agreement between both products is present for the maximum levels amplitude range (Fig. 4). However, the model (Fig. 4b) appears to exaggerate the reproduction of

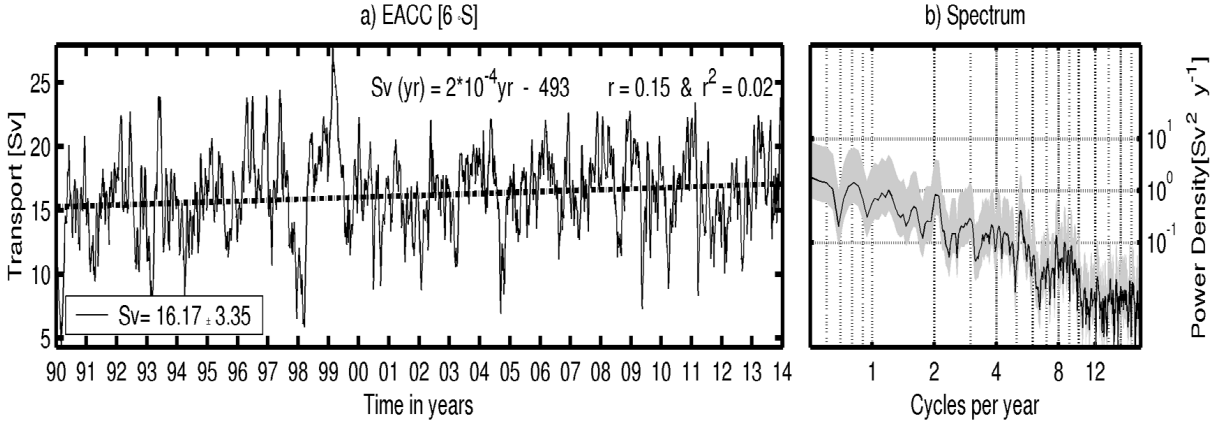

Figure 3. Model derived time-series of the volume transport (Sv) of the EACC, vertically integrated in the upper 500 m below the sea surface (a), and its b) power-spectrum (Sv^2 $year^{-1}$) estimated using the multi-taper method, computed at 6°S, across the width of the current between 39.5 and 40.5°E. The dashed-line represents the linear trend following the equation Sv (yr) = $2x10^{-4}$yr – 493, with correlation coefficient (r), and coefficient of determination (r^2). The grey envelope highlights the standard deviations around the mean signal (black line).

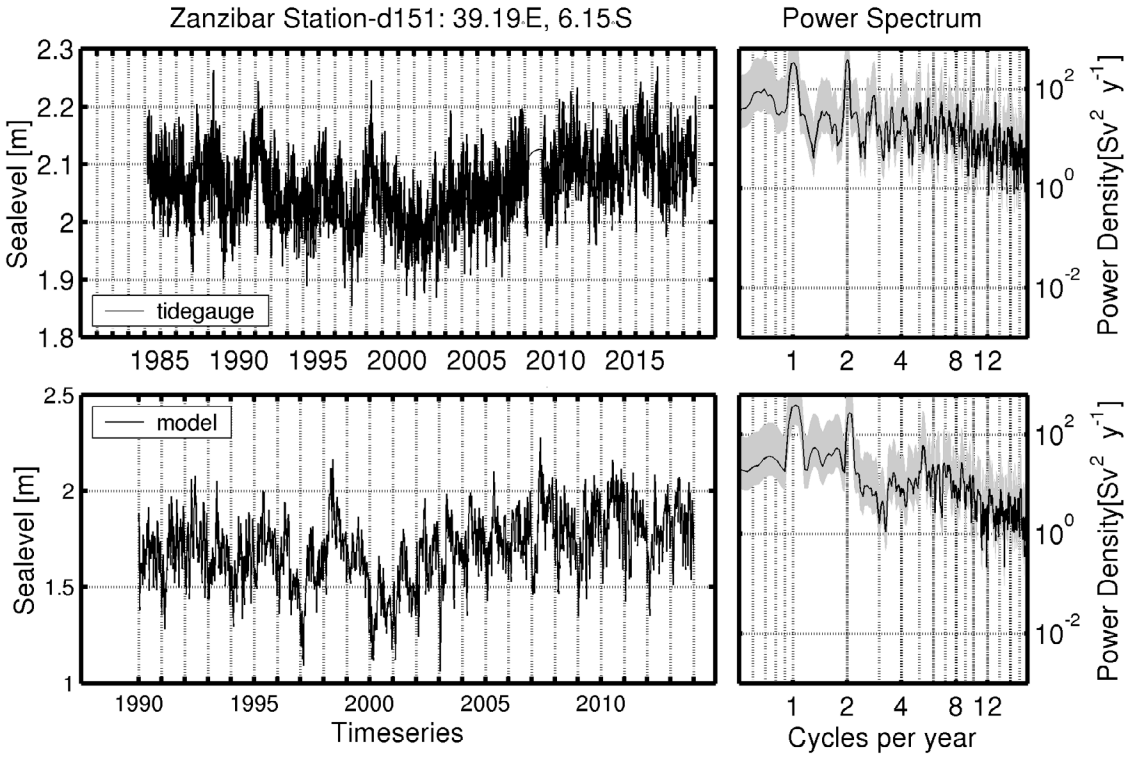

Figure 4. Data (upper panel) and Model (lower panel) comparison for the sea-level variation (m) at a tide-gauge mooring site located in Zanzibar. The observed data has been extracted from University of Hawaii Sea-level Center, and spans from 1984 to 2018. The model time-series spans from 1990 to 2013. The left panels show the inter-annual variations, and the right panels show their corresponding power-spectra (Sv^2 year^{-1}) computed using the multi-taper approach. The grey envelope highlights the standard deviations around the mean signal (black line).

lower bound amplitudes of the signals, where its minimum reached nearly 1 m. On the other hand, the observational data has barely reached a minimum amplitude of 1.85 m (Fig. 4a). It is not surprising as the model sea surface height (SSH) used here is an absolute parameter (i.e. the changes in SSH is with respect to a fixed absolute reference frame, e.g. earth's center). Additionally, the sea-level as observed by the tide-gauge is a relative (i.e. is measured locally relative to the land), and is thus the sum of absolute sea level changes and vertical motions of the land, heavily impacted by geological activities. Nevertheless, in spite of such apparent discrepancies, it is remarkable to note that both products have reproduced identical power-spectra profiles across the whole scales of variabilities. The strongest signals were distinctly characterized by both annual and semi- annual frequencies, identified by peaks of one cycle per year and two cycles per year, respectively. It is likely that these predominant peaks are related to the seasonal reversal of the monsoons, which creates two seasons. Furthermore, both products also reproduce vigorous inter-annual (frequency < 1 cycle year^{-1}) and intra-seasonal events (frequency > 8 cycles year^{-1}), with a consistent decreasing slope towards lower energy levels. There is also a relatively strong variability at frequency of 4 - 5 cycles year^{-1}, which could possibly suggest mesoscale activity identified by Gamoio *et al.* (2017).

Chlorophyll-*a*

The observed and modelled monthly climatology of sea surface chlorophyll-*a* concentrations are presented in Fig. 5 and Fig. 6 respectively. Both model and observations reveal that higher chlorophyll-*a* concentrations are generally confined closer to the coast (presumably over the narrow continental shelf), and lower concentrations are located slightly offshore, throughout the annual cycle (i.e. January to December). Both products also suggest that the lowest concentration of chlorophyll-*a* in the whole domain scale occurs in January. It is not clear why such a pattern is presented, as it stands in stark contrast with the distribution in the preceding month and the month thereafter (i.e. December and February). While both the model and observations show consistently comparable spatial and temporal patterns for relatively higher levels of chlorophyll-*a* concentration, it is also noticeable that the model has struggled to reproduce lower levels in

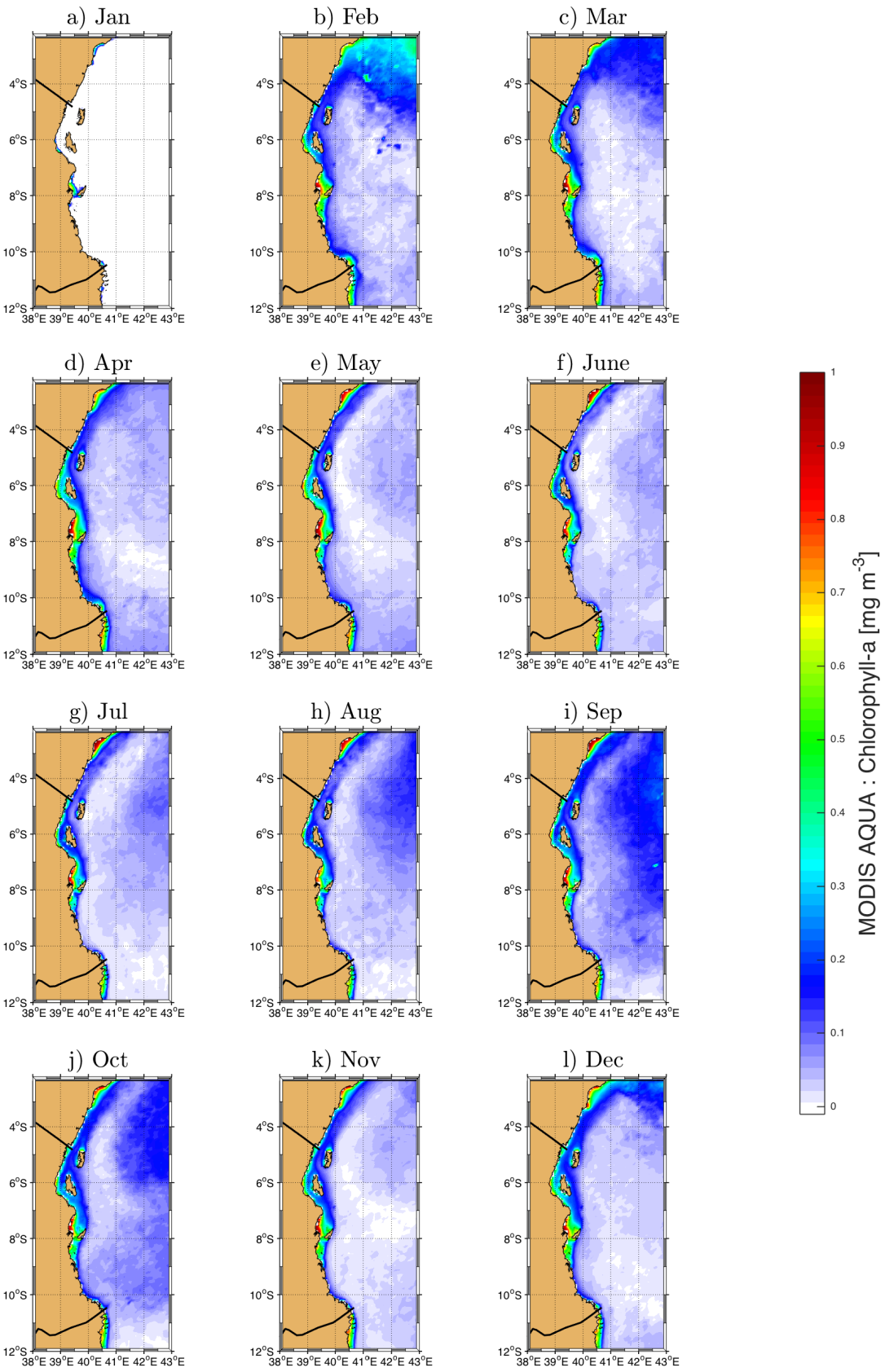

Figure 5. Surface maps of the MODIS-AQUA satellite-derived monthly climatologies of the estimated chlorophyll-*a* concentrations (mg m^{-3}) throughout the annual cycle along the coasts of Tanzania and Kenya.

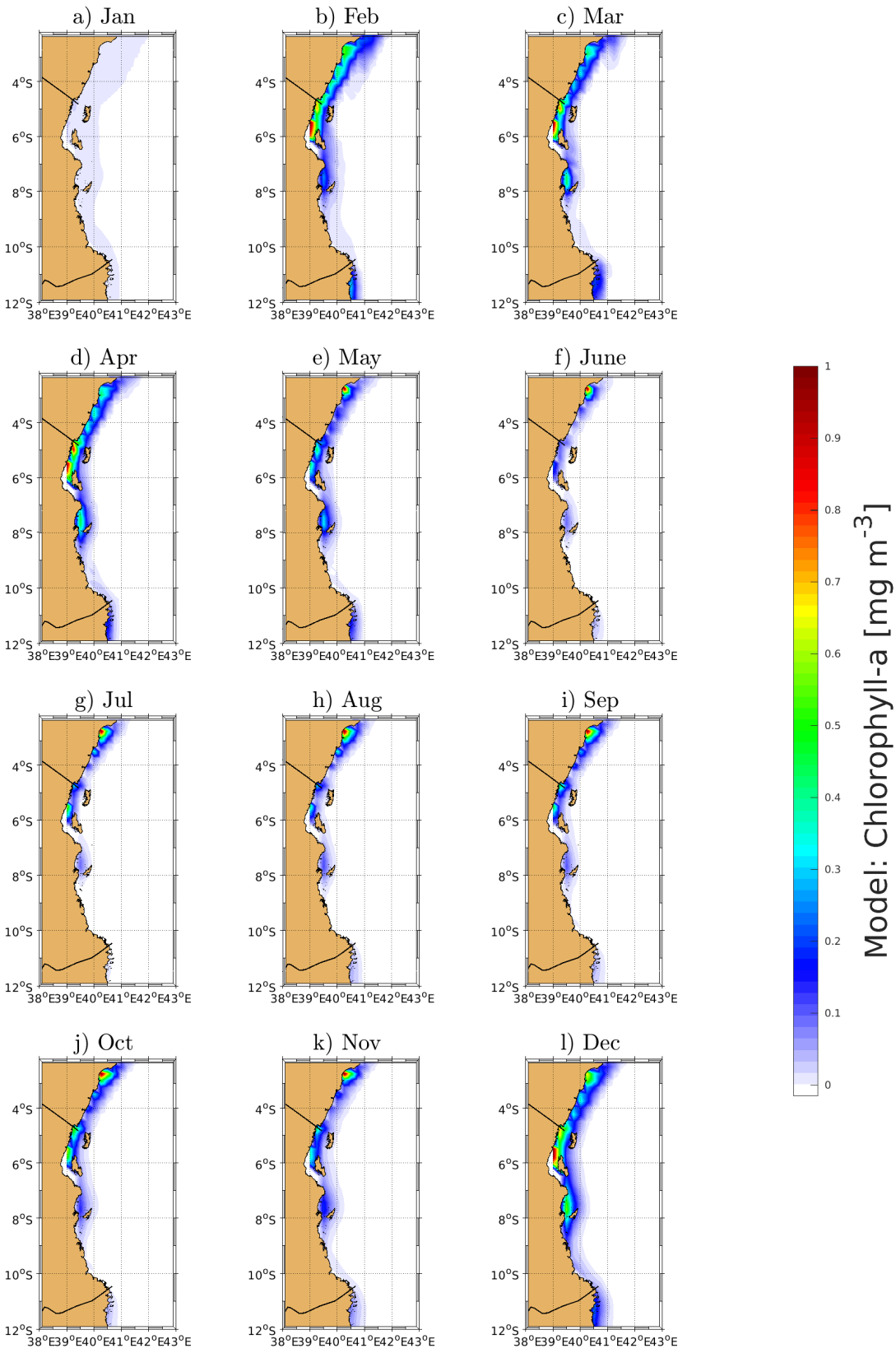

Figure 6. Surface maps of the model-derived monthly climatologies of the estimated chlorophyll-*a* concentrations (mg m^{-3}) throughout the annual cycle along the coasts of Tanzania and Kenya. Notice that at specific locations within the Zanzibar Channel the model grid resolution struggled to reproduce chlorophyll-*a* concentrations. This could correspond to shallower areas in the channel.

chlorophyll-*a* concentrations in the offshore environment. Nevertheless, the model appears to reproduce the biological property investigated reasonably well.

Fig. 6 will be revisited in the results section and discussed in light of the model derived surface maps of the Ekman upwelling index.

4. Results and Discussion

Spatial and temporal variation of the model derived Ekman upwelling

To investigate the nature and characteristics (i.e. spatial and temporal variabilities) of the upwelling events along the Tanzanian and Kenyan coasts, the surface spatial expressions of the upwelling phenomenon were computed and mapped, calculated through estimates of the Ekman vertical velocities (Ekman pumping and suction), derived from the meridional wind-stress vector (τ), scaled by the cross-shore horizontal length scale of the upwelling Lu (width of Ekman divergence), following the formula derived by Bakun (1973), as presented in Marchesiello and Estrade (2010) (see Equation 2).

It is important to mention that the horizontal grid resolution has been used in the equation instead of the commonly used Rossby radius of deformation, which in the region of interest ranges between about 100 km in the south and 230 km in the north (Chelton *et al*., 1998). The use of finer grid resolution has been suggested (Capet *et al*., 2004), because it has been diagnosed that the Rossby radius usually over-estimates the magnitude of the upwelling rate (Capet *et al*., 2004; Marchesiello and Estrade, 2010). In Equation 2, a positive (negative) U denotes an Ekman suction (pumping), indicative of upwelling and downwelling events respectively. Fig. 7 shows the results (monthly climatologies) throughout the year cycle. It suggests that upwelling events along the coasts of Tanzania and Kenya are highly variable, but a normal occurrence.

Throughout the annual cycle it is apparent that stronger upwelling events (Ekman suction) occur on-shore almost along the whole coastal zone, and offshore downwelling (Ekman pumping; more to the north of 6°S than in the south) is persistent from December to February (Fig. 7a,b,l). It is important to mention that this is the period dominated by the Northeast Monsoon winds. During this period an exception is observed in a narrow zonal strip that extends between northern Pemba Island and the African mainland, lying exactly at the border between Tanzania and Kenya, where a downwelling event (Ekman pumping) is persistent. During the dominant on-shore downwelling period along the coast observed mostly from July to October (Fig. 7g and 7j), this zonal band switches to a persistent upwelling dominated region. It is also important to mention that the period spanning from July to October is characterized by the Southwest Monsoon winds. During the month of June (Fig. 7f), upwelling is more prevalent both on-shore and offshore, except at a locality (3 - 4.5°S) to the south of Kenya.

The results presented here clearly indicate the dominant occurrence of coastal upwelling during the Northeast Monsoon and downwelling during the Southwest Monsoon, which suggests a seasonal dependence. Nevertheless, the occurrence of isolated small patches of upwelling events during the Southeast Monsoon, and downwelling during the Northeast Monsoon may suggest that not all observed coastal upwelling events present in Fig. 7 are driven by the same physical process, such as wind-stress curl.

Spatial and temporal variation of the model derived chlorophyll-a

To determine the biological response in the upwelling area, the model- derived surface monthly climatologies of chlorophyll-a concentrations was again inspected. As previously indicated, Fig. 6 shows spatial and temporal distribution during a full annual cycle. As with the upwelling events (Fig. 7), it is notable that chlorophyll-*a* also shows high levels of spatial and temporal variabilities along the Tanzanian and Kenyan coasts. The model suggests higher concentrations along the coast in December (Fig. 6l), and from February to April (Fig. 6b to 6d). On the other hand, lower concentrations are more notable in January (Fig. 6a), and from June to September (Fig. 6f to 6i) respectively. It is evident that there are higher concentrations of chlorophyll-*a* during the inter-monsoon period from the Northeast Monsoon to the Southwest (March - April) than that from Southwest to Northeast (October - November).

One should note that higher surface chlorophyll-a distribution presented in Fig. 6 does not necessarily co-occur with the higher distribution patterns of upwelling events as suggested in Fig. 7. Their confinement to the coast could suggest potential contribution of land-based material flushed into the sea by the rivers and streams. This may lead to the conclusion that the biological responses observed in the region could be a consequence of both upwelling events and river discharges.

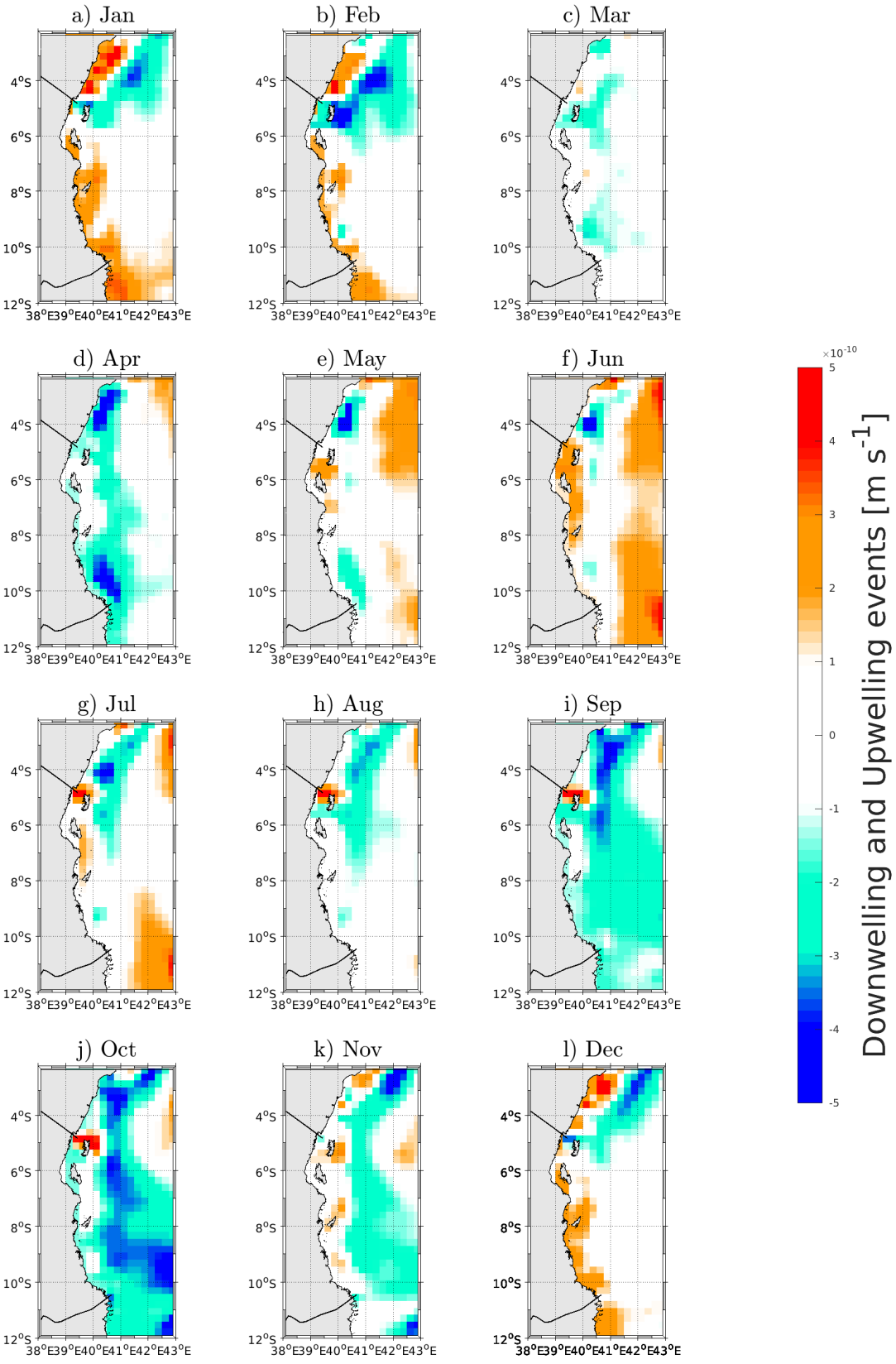

Figure 7. Surface maps of the model-derived monthly climatologies of the upwelling and downwelling velocities (m s^{-1}) estimated using Equation 2. Positive (negative) are indicative of upwelling (downwelling) events respectively, along the coasts of Tanzania and Kenya.

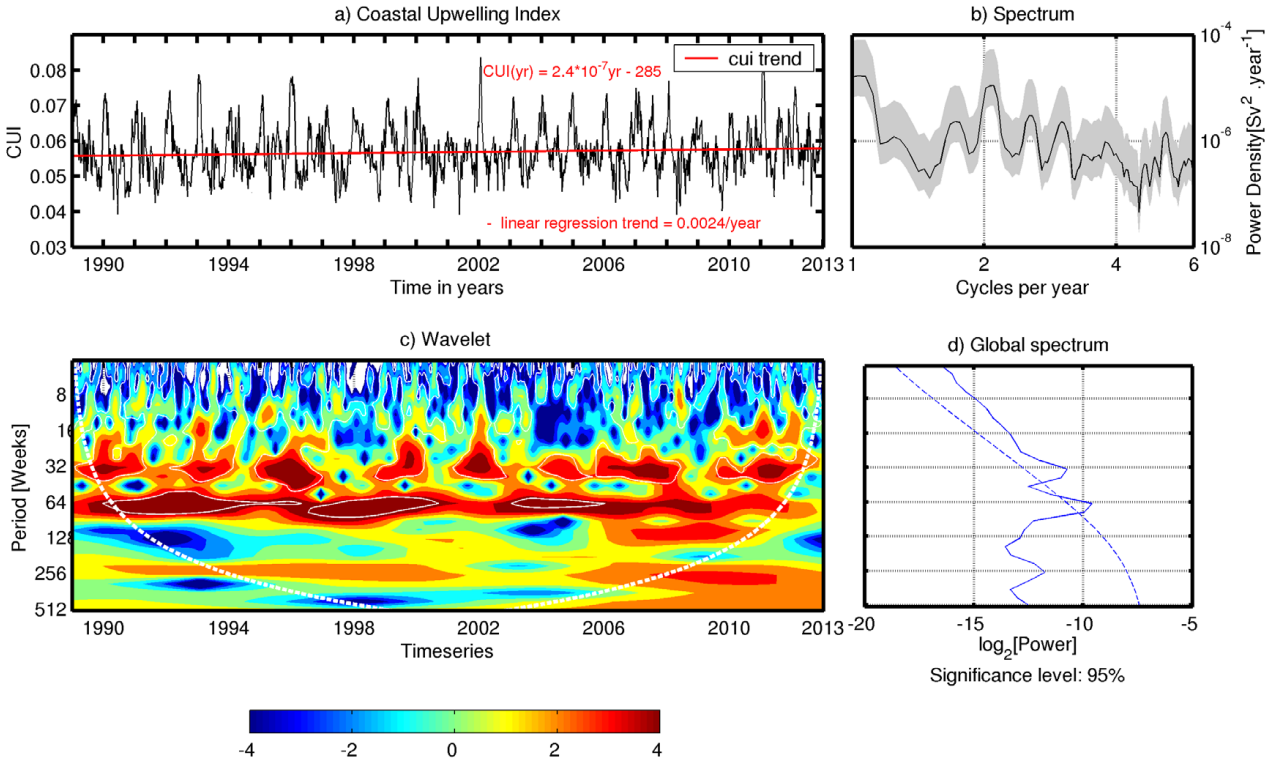

Figure 8. a) Model-derived time-series of the coastal upwelling index (CUI) (unitless) estimated from the sea surface temperature (SST) off the coastal city of Tanga in Tanzania, and b) its associated power density spectrum (Sv^2 $year^{-1}$) estimated using the multi-taper approach. Panels c) and d) show the wavelet of the CUI and its power spectrum respectively. The red line in a) shows the linear trend of the CUI from 1990 to 2013, with annual rate (0.0024/year ≃ 4%) which follows the equation CUI (yr) = 2.4x10^{-7}yr - 285. The dashed line in d) shows the confidence line at 95 %.

SST upwelling index in Tanga

To assess the long-term variability of the upwelling events, the CUI time-series, its power density spectrum, as well as the wavelet transform and its global power spectrum were computed and are presented in Fig. 8. As can be observed in Fig. 8a, the CUI shows high levels of variability with its fluctuating peaks ranging between 0.04 and 0.08. The higher peaks suggest a dominance of an inter-annual variability. In fact, inspection of its power density spectrum computed using the multi-taper approach (Fig. 8b), shows two most dominant peaks of temporal variability, located annually and semi-annually (1 cycle $year^{-1}$ and 2 cycles $year^{-1}$ respectively). The latter could be related to the seasonal reversal of the monsoons (2 monsoons per year) that are known to have a strong influence over the dominant modes of variability in the WIO. In order to inspect other variability patterns, a wavelet signal was analyzed (Fig. 8c). The year versus period plot shows two dominant structures occurring with a periodicity of nearly 32 and 64 weeks. The white dashed line shown in Fig. 8c bounds within it all information which is weighted at a confidence level of 95 %. A notable pattern observed is an intermittent (discontinuous) regular pulse throughout the time-series along a 32-week period, and another continuous pulse at a 64-week period, indicative of inter-annual variability. Their global power spectrum (Fig. 8d) also suggests that the most dominant mode of variability is the inter-annual mode, followed by the seasonal mode.

When a linear regression trend line is fitted onto the time-series of CUI (Fig. 8a), it reveals an overall small upsloping profile that follows the equation CUI(yr) = 2.4x10^{-7}yr – 285, which suggests that the CUI is slowly intensifying over the years, at a rate of 0.0024 $year^{-1}$ ≃ 4% of the yearly averaged increase. It is likely that this increasing trend can be explained by the observed weak trends of intensification of the wind system in the region (Mahongo *et al.*, 2012), also recently documented by Garcia-Reyes *et al.* [this issue]. Interestingly, the calculated value (0.0024 $year^{-1}$) is comparable with the annual trend estimates (0.002 $year^{-1}$) of another SST based coastal upwelling index derived by Leitão *et al.* (2019), along the Portuguese coast, using remote sensing data (See their Table 3), spanning the years 1985 to 2009.

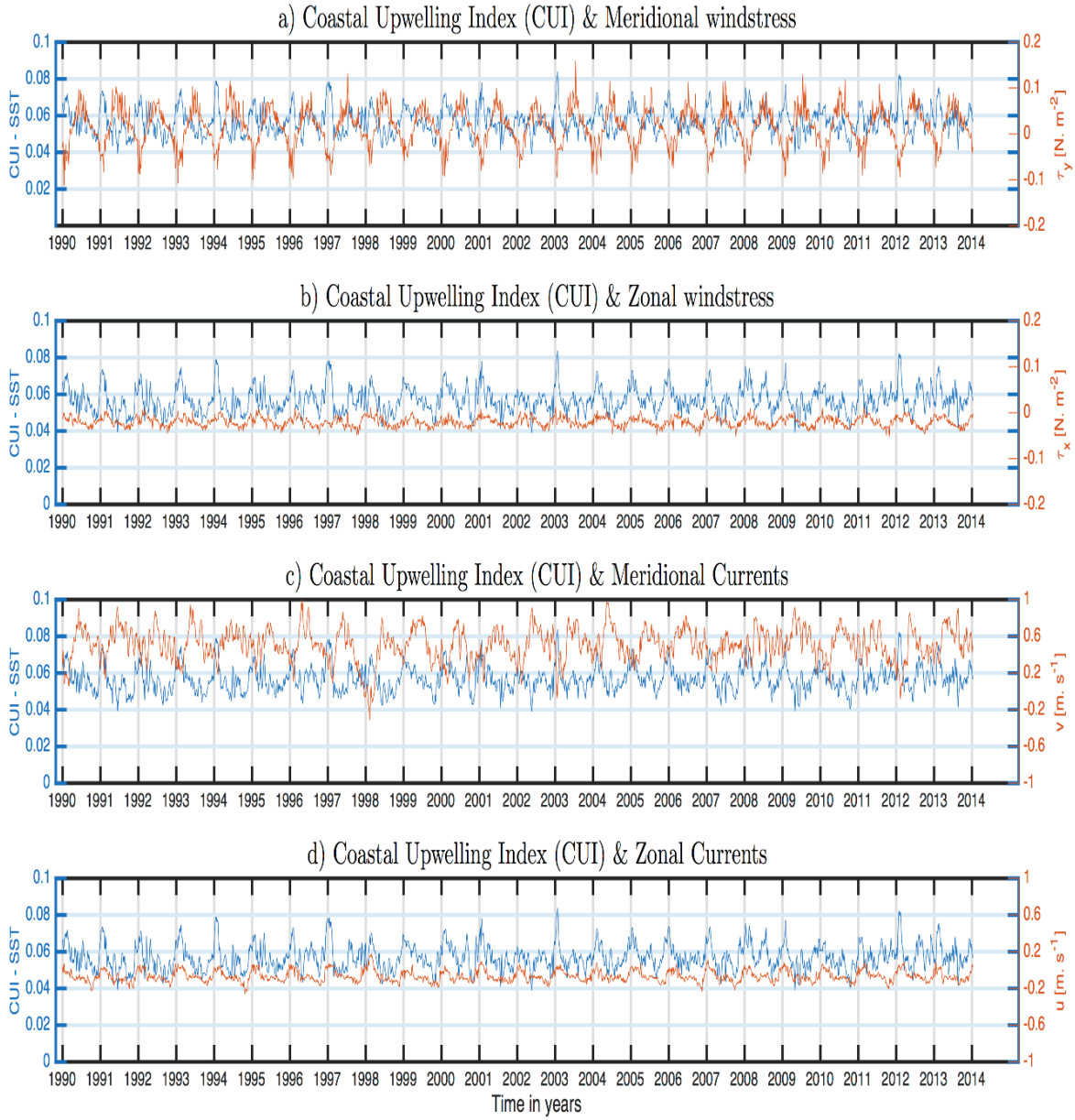

Figure 9. Model-derived time-series of the SST coastal upwelling index (CUI) (blue line) (unitless) and a) meridional, b) zonal components of the wind-stress (N m^{-2}); and c) meridional, d) zonal components of the ocean surface currents (m s^{-1}). For reference see the box positions in Figure 1, used to derive the index.

Relating winds and currents to the SST upwelling index

To assess the relation between the CUI and atmospheric/oceanic forcing in the EACC region, the model derived time-series of the meridional (τy) and zonal (τx) components of the wind-stress, and ocean surface currents (*v* and *u*) respectively, averaged across the width of the EACC at 6°S (for reference see Fig. 1) were computed, and subsequently, compared against the variability of the CUI derived above. The results are shown in Fig. 9. With regards to the meridional components of the flows, positive (negative) values denote northward (southward) directions respectively. Whereas for zonal components, positive (negative) values indicate eastward (westward) directions respectively.

Fig. 9a reveals a general increase of the CUI, each time coinciding with an intensification of the southward component of the wind-stress (negative τy). It is also evident that the CUI decreases with an intensification of the northward component of the wind-stress (positive τ*y*). These results clearly suggest that the upwelling is more developed during the Northeast Monsoons (when the winds are southward oriented), as opposed to

the period of the Southwest Monsoon (when the winds are northward oriented). This finding is in agreement with the patterns presented in Fig. 7. To quantify these facts, the statistical correlations between these parameters were performed, and the regression through the scatter plots, and also the strengths of the correlation coefficients (r) analysed, as presented in Fig. 10. Fig. 10a shows a significant ($p < 0.05$), moderate negative linear relationship ($r = -0.53$) between the CUI and the meridional wind-stress τy, suggesting that the τy controls about 28 % of the upwelling variability. On the other hand, no significant relation was found with τx. The correlation ($r = 0.22$) is weak between the CUI and τx (Fig. 10b).

Inspecting Fig. 9c, it is further noticed that CUI has consistently exhibited decreased (increased) tendency each time when the meridional northward current (EACC) velocity increased (decreased) its intensity (Fig. 9c). As would be expected, it is during the Southwest Monsoon when the EACC is strongly intensified in response to the southwest winds, thus both flows (winds and currents) propagate northward (Nyandwi, 2013). On the other hand, a more direct relationship translated by an increased (decreased) tendency of the CUI, equally resulted in an increased (decreased) zonal velocity component of the oceanic currents (Fig. 9d). Statistical analysis in Fig. 10 indicated a low negative ($r = -0.40$, $p<0.05$) linear relationship with a steep slope between the upwelling and the meridional current (v)(Fig. 10-c). It is not clear what the main reason for this could be. However, one may argue this is related to the narrow range of the prevailing local windstress variations. On the other hand, there was a significant ($p<0.05$) and moderate positive ($r = 0.52$) relationship (Assuero *et al.*, 2006), between the upwelling and the zonal components of the current (u), even at very weak current intensities, which ranged around ± 0.2 ms^{-1} (Fig. 10d). This suggests that the reversals of the EACC in an onshore and offshore direction make a significant contribution to the upwelling variability.

Cross-shore structure of the EACC at 5°S during an upwelling event

To assess the characteristics of the upwelling through the water column with relation to the EACC, an

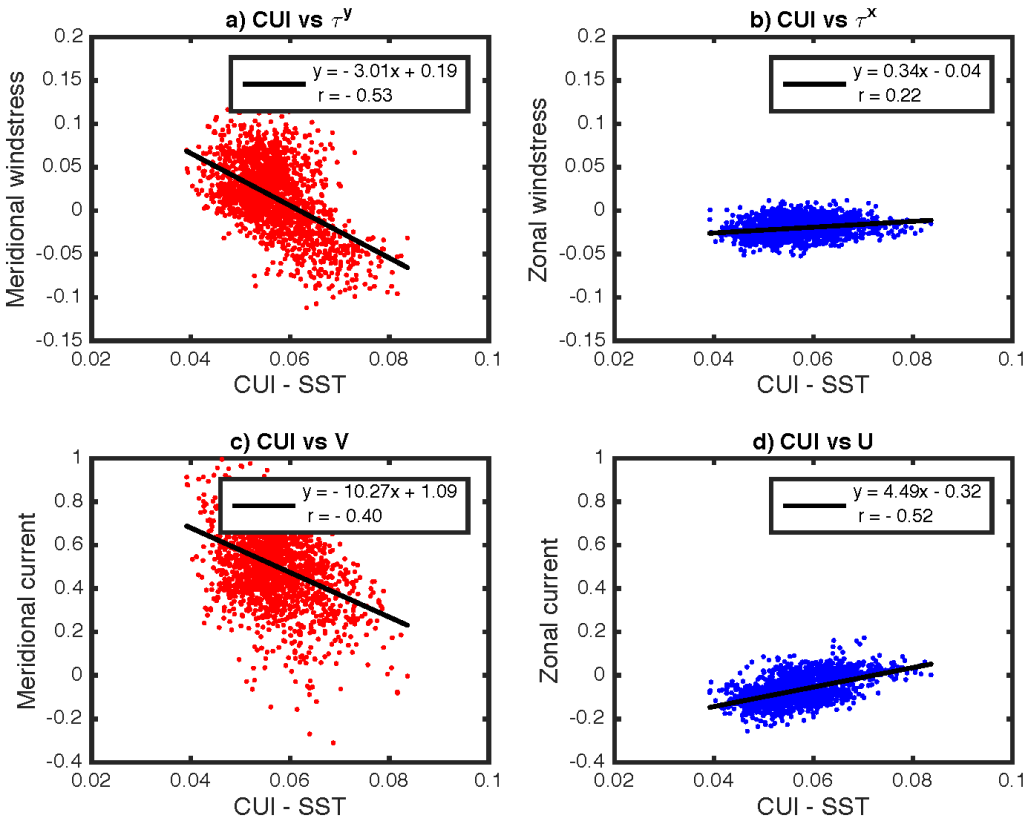

Figure 10. Scatter plots of model-derived Pearson correlations between SST coastal upwelling index (CUI [unitless]) against both wind-stress [N. m^{-2}], a) meridional, b) zonal components, and ocean currents [m. s^{-1}] c) meridional, d) zonal components respectively, along the coast. It also includes the best fit of the linear relationship (y), and correlation coefficients (r), estimated at 95 % confidence.

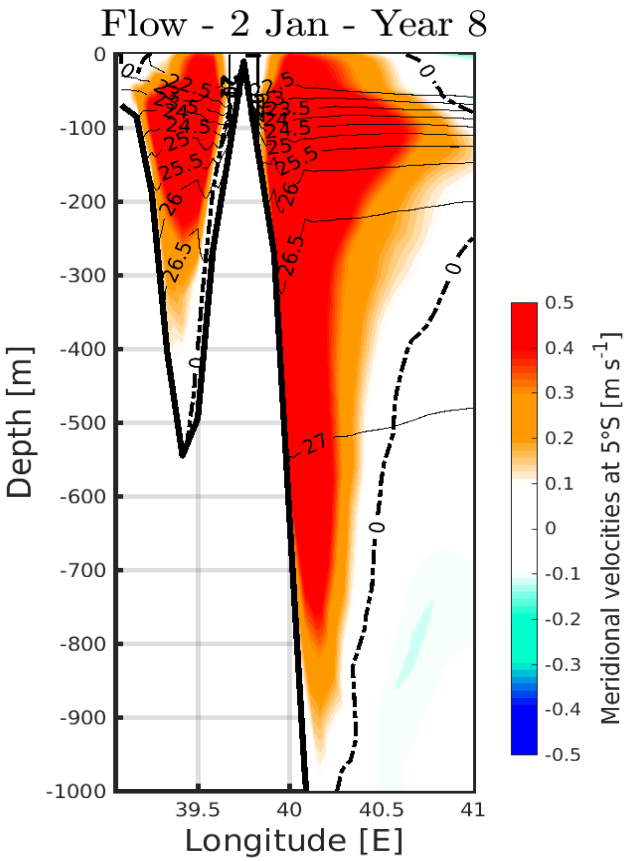

Figure 11. Cross vertical section of the model-derived instantaneous meridional flow in m s^{-1}, during an active upwelling event on the 2 January Year 8, at 5°S, over a distance spanning from 39 to 41°E. The positive (negative) values indicate northward (southward) directions respectively. The black contours represent the isopycnals (in kg m^{-3}) at 0.5 intervals.

instantaneous active upwelling event during the Northeast Monsoon season, occurring on the 2nd of January, model year 8 was selected, and the flow density structure portrayed by the velocity, temperature and salinity properties was inspected. Meridional flow overlaid by potential density is presented in Fig. 11, while potential temperature and salinity is presented in Fig. 12a and Fig. 12b respectively. Positive (negative) values in Fig. 11 denote a northward (southward) direction of propagation, respectively.

Fig. 11 shows two cores of the northward EACC located inshore and offshore. The main core of the inshore flow is approximately between 39.2 and 39.6°E, while the offshore core is between 39.9 and 40.9°E. The inshore core lies within the Pemba Channel, and nearly spans the whole width of the Channel. It has a core velocity of about 0.8 m s^{-1}, located almost at the center of the Channel at about 100 m below the sea surface (Fig. 11). A minimum velocity of about 0.1 m s^{-1} is observed at a maximum depth of about 400 m below the sea-surface. On the other hand, the offshore core appears more strongly intensified, with maximum velocities reaching 1 m s^{-1}, lying along the continental slope, at about 100 m below the sea-surface. This offshore core is deep reaching, with minimum velocities of about 0.1 m s^{-1} been observed at depths beyond 950 m below the sea-surface (Fig. 11). This pattern of circulation is consistent with the description shown in Fig. 1, and that published by Mahongo and Shaghude (2014), and Mayorga-Adame *et al.* (2016), which support the concept of branching-off of the EACC and recirculation of the flow field around the Zanzibar archipelago. One should note that within the Pemba Channel there is a southward flow (negative values) attached to the eastern boundary slope of the Channel, and it extends throughout the Channel's depth, where it reaches a maximum depth of about 500 m. On the western side of the Channel it is confined only on the upper ~ 30 m, over the shelf. This flow pattern characterized by a northward flow along the continental slope offshore (i.e. eastern flank of the Pemba Island), and a southward flow on-shore (i.e. western flank of the Pemba Island), is a typical characteristic of an anticyclonic recirculation around the Island. Roberts (2015) has indicated that upwelling can be generated by island-wake processes in the region, which usually triggers a pattern similar to that observed in Fig. 11.

Consistently, potential temperature patterns in Fig. 12a reveals uplifting of the isotherms within the Pemba Channel; more notable beyond depths of about 100 m below the sea surface. Conversely, there is evidence of deepening of the isotherms above the 100 m below the sea surface. This suggests the occurrence of a sub-surface upwelling event. Offshore (east of 40°E), along the continental slope, uplifting of the isotherms are more intensified below the depth of 500 m. On the other hand, between the depths of about 50 m and 200 m, the isotherms are nearly zonal and more tightly close together, revealing a relatively strong temperature gradient (Fig. 12a), suggesting a higher stratification. Between 200 m and 500 m depth the isotherms are uplifted offshore and downwelled closer to the continental slope. The isopycnals shown in Fig. 11 also consistently show a similar pattern. This could potentially suggest an inflow of the offshore water toward the coast, as indicated by the isopycnal topography.

Salinity distribution in Fig. 12-b reveals the presence of localized maximum salinity values greater than 35.2 PSU within the Pemba Channel, centered at a depth of about 100 - 150 m below the sea surface. This could

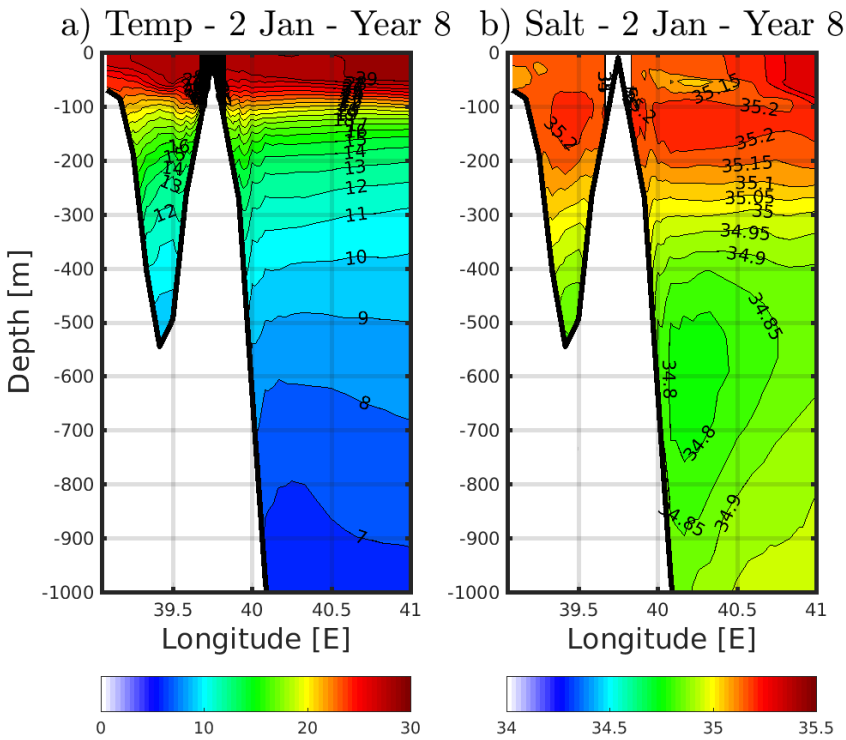

Figure 12. Cross vertical section of the model-derived instantaneous hydrographic properties a) temperature (°C) and b) salinity (PSU), during an active upwelling event on the 2 January Year 8, at 5°S, over a distance spanning from 39 to 41°E.

explain the convergence of the isopycnals towards the 100 m layer observed in Fig. 11. It could also possibly explain the blockage of upwelling evolution to reach the sea surface. Thus, stratification appears to be a limiting factor. Looking at the salinity distribution at the offshore environment, it is notable that these high-salinity values are also present at the sea surface to the east of 40.4°E. Here it appears to sink to depths of about 100 m, and then propagates towards the coast between 100 m and 200 m depth. This further corroborates the possibility of a sub-surface westward flow suggested by the westward deepening of the isotherms (Fig. 12a), and slanted isopycnals and velocities in Fig. 11. The modelling study by Manyilizu *et al.* (2014) also revealed an intrusion of offshore tropical western Indian Ocean waters into the Tanzanian coast, dominated by variability on a time-scale of about 5 years.

Conclusion

In this study a coupled biophysical climatological model and a physical inter-annual simulation run from 1990 to 2013 were used to simulate the upwelling events along the East African coast, off Tanzania and Kenya. The models were able to simulate the circulation and spatial and temporal upwelling variabilities reasonably well, when compared to documented information and in-situ hydrographic measurements. The time-series over the 23 years of the vertically integrated volume transport of the EACC at 6°S on the upper 500 m below the sea surface, plus inspections of its power-spectrum, revealed a consistent positive northward transport, suggesting that the current circulation is permanently northward, regardless of the season, and it is characterized by strong modes of variabilities ranging from intra-seasonal to inter-annual and longer time-scales. This is consistent with the results from previous studies (Swallow *et al.*, 1991; Nyandwi, 2013; Manyilizu *et al.*, 2016).

Surface maps of monthly climatologies of the Ekman derived upwelling phenomena throughout the annual cycle suggested that upwelling along the coasts of Tanzania and Kenya is a normal occurrence. It was manifested more strongly in terms of its intensity and spatial coverage over the east African continental shelf between December and February, which suggests its predominance during the Northeast Monsoon season (Fig. 7a, 7b, 7l). The presence of a persistent localized and small extension of an upwelling cell to the north of Tanzania, around Tanga City, from May to November (period of the Southwest Monsoon, Fig. 7e to 7h), suggests that this upwelling could be driven by a different dynamic process as opposed to that observed during the other season (Fig. 7a, b, l). It is likely that instabilities

of the EACC around the chain of islands (Mafia, Unguja, Pemba), and along the continent's lateral boundary play a strong role in creating these upwelling cells, as suggested by direct measurements of the flow field presented by Roberts (2015). In fact, time-series of a SST-based coastal upwelling index suggests both meridional southward winds and zonal variations of the flow along the EACC strongly correlate with the occurrence of the upwelling events by 28% and 27% respectively (Fig. 10). Trend analysis of the coastal upwelling index has shown a small increase (0.0024 year^{-1} ≃ 4%) during the whole modelled period spanning from 1990 to 2013 (Fig. 8a). It is likely that such an increase is related to the general intensification of the volume transport (Fig. 3), and wind system and ocean currents (Mahongo *et al*., 2012; Garcia-Reyes *et al*. [this issue]).

Both wavelet and multi-taper techniques (Fig. 8b, d) also revealed a wide spectral range of the upwelling frequency variability, with dominant signals at inter-annual time-scales. Chlorophyll-*a* distribution patterns in time and space (Fig. 6) suggested that chlorophyll-*a* availability and variability could be modulated by both upwelling events and continental discharges via runoff fluxes. Nevertheless, fundamental questions to assess how the physical processes interact with biological production still need to be answered through future studies.

Acknowledgements

The authors are very grateful for the funding provided by WIOMSA via a MASMA grant, and the IOC Africa for this study. The model simulation was performed in the department of Conservation and Marine Science, Cape Peninsula University of Technology, South Africa. Special gratitude to Pierrick Penven (IRD - Brest, France) for providing the boundary conditions for the inter-annual model simulation.

Many thanks also are dedicated to both the reviewer and guest-editor for their tireless contributions to improve the quality of the manuscript. Thanks to the PEACC team for their enthusiastic support in table discussions at various harmonization meetings.

References

Asuero AG, Sayago A, González AG (2006) The correlation coefficient: An overview. Critical Reviews in Analytical Chemistry 36 (1): 41-59 [doi:10.1080/10408340500526766]

Backeberg BC, Penven P, Rouault M (2012) Impact of intensified Indian ocean winds on mesoscale variability in the Agulhas system. Nature Climate Change 2: 608–612 L04604 [doi:10.1038/NCLIMATE1587]

Bakun A (1973) Coastal upwelling indices, west coast of North America. Technical reports 1946 - 71. U. S. Department of Commerce, NOAA Technical Report. NMFS. SSRF. 671pp

Bakun A (1998) Ocean triads and radical interdecadal stock variability: bane and boon for fisheries management. In: Pitcher T, Hart PJB, Pauly D (eds) Reinventing fisheries management. Chapman and Hall, London, UK. pp 331-358

Brink KH, Halpern D, Huyer A, Smith RL (1983) The physical environment of the Peruvian upwelling system. Progress in Oceanography 12: 185-305

Caldwell PC, Merrifield MA, Thompson PR (2015) Sea level measured by tide gauges from global oceans - the Joint Archive for Sea Level holdings (NCEI Accession 0019568, version 5.5. Technical report, NOAA, National Centers for Environmental Information, USA, 42 pp. [doi:10.7289/V5V40S7W]

Capet XJ, Marchesiello P, McWilliams JC (2004) Upwelling response to coastal wind profiles. Geophysical Research Letters 31: L13311 [doi:10.1029/2004GL020123]

Chelton DB, deSzoeke RA, Schlax MG, Naggar KE, Siwertz N (1998) Geographical variability of the first- baroclinic rossby radius of deformation. Journal of Physical Oceanography 28: 433-460

Colas F, McWilliams JC, Capet X, Kurian J (2012) Heat balance and eddies in the Peru-Chile current system. Journal of Climate, Dynamics 39: 509-529 [doi: 10.1007/s00382-011-1170-6]

Collins C, Reason CJC, Hermes JC (2012) Scatterometer and reanalysis wind products over western Tropical Indian Ocean. Journal of Geophysical Research 117: C03045

Conkright ME, Locarnini RA, Garcia HE, O'Brien TD, Boyer TP, Stephens C, Antonov JI (2002) World ocean atlas 2001: Objective analyses, data statistics, and figures, CD-ROM documentation. Technical Report, National Oceanographic Data Center, Silver Spring, MD, 392 pp

Cury P, Roy C (1989) Optimal environmental window and pelagic fish recruitment success in upwelling areas. Canadian Journal of Fisheries and Aquatic Sciences 46: 670-680

Da Silva AM, Young CC, Levitus S (1994) Atlas of surface marine data 1994, Vol. 1, algorithms and procedures. Technical Report, U. S. Department of Commerce, NOAA, 83 pp

Dai A, Qian T, Trenberth K, Milliman JD (2009) Changes in continental freshwater discharge from 1948 to 2004. Journal of Climate 22: 2773-2792 [doi: 10.1175/2008JCLI2592.1]

Debreu L, Marchesiello P, Penven P, Cambon G (2012) Two-way nesting in split-explicit ocean models: Algorithms, implementation and validation. Ocean Modelling 49-50: 1-21 [doi: 10.1016/j.ocemod.2012.03.003]

Demarcq H, Faure V (2000) Coastal upwelling and associated retention indices derived from satellite SST. Applications to *Octopus vulgaris* recruitment. Oceanologica Acta 23: 391-408

Durand M-H, Cury P, Mendelssohn R, Roy C, Bakun A, Pauly D (1998) Global versus local changes in upwelling systems. Editions ORSTOM, Paris, France. 558 pp

Echevin V, Marchesiello P, Penven P (2005) Modelisation des regions d'upwelling de bord est a l'aide du systeme Mercator. La lettre trimestrielle Mercator Ocean 18: 18-22

Fasham MJR, Ducklo, HW, McKelvie SM (1990) A nitrogen-based model of plankton dynamics in the oceanic mixed layer. Journal of Geophysical Research 48: 591-639

Gamoio M, Reason C, Collins C (2017) A numerical investigation of the Southern Gyre. Journal of Marine Systems 169: 11-24

Garcia-Reyes M, William JS, David SS, Bryan AB, Albert JS, Steven JB (2015) Under pressure: Climate change, upwelling, and eastern boundary upwelling ecosystems. Frontiers in Marine Science 2 (16): 109 [doi: 10.3389/fmars.2015.00109]

Garcia-Reyes M, Mahongo S (2020) Present and future trends in winds and SST off Central East Africa, [this issue], WIO J. Marine Science.

Gruber N, Frenzel H, Doney SC, Marchesiello P, McWilliams JC, Moisan JR, Oram G-KP, Stolzenbach KD (2006) Simulation of phytoplankton ecosystem dynamics in the California Current System. Deep Sea Research Part I 53 (9): 1483-1516

Leitão F, Vânia B, Vieira V, Silva PL, Relvas P, Teodósio MA (2019) A 60-year time series analyses of the upwelling along the Portuguese coast. Water 11 (1285): 1-26 [doi:10.3390/w11061285]

Lett C, Penven P, Ayon P, Freon P (2007) Enrichment, concentration and retention processes in relation to anchovy (*Engraulis ringens*) eggs and larvae distributions in the northern Humboldt upwelling ecosystem. Journal of Marine Systems 64: 189-200

Mahongo, Francis J, Osima SE (2012) Wind patterns of Coastal Tanzania: their variability and trends. Western Indian Ocean Journal of Marine Science 10(2): 107-120

Mahongo BS, Shaghude YW (2014) Modelling the dynamics of the Tanzanian coastal waters. Journal of Oceanography and Marine Science 5 (1): 1-7 [doi:10.5897/joms2013.0100]

Manyilizu M, Dufois F, Penven P, Reason CJC (2014) Inter-annual variability of sea surface temperature and circulation in the tropical western Indian Ocean. African Journal of Marine Science 36 (2): 233-252 [doi: 10.2989/1814232X.2014.928651]

Manyilizu M, Penven P, Reason CJC (2016) Annual cycle of the upper ocean circulation and properties in the tropical western Indian Ocean. African Journal of Marine Science 38 (1): 81-99 [doi: 10.2989/1814232X.2016.1158123]

Manyilizu M, Sagero P, Halo I, Mahongo S (2020) Inter-annual relationship of SST and upper-ocean circulation between northern Tanzania and northern Kenya Bank [This issue], WIO J. Marine Science.

Mapunda XE (1983) Fisheries economics in the context of the artisanal fisheries of the marine sector. Technical report, TAFIRI. SWIOP Document OISO. RAF/79/065/WP/7/83, 6 p

Marchesiello P, Estrade P (2010) Upwelling limitation by inshore geostrophic flow. Journal of Marine Research 68: 37-62

Mayorga-Adame CG, Ted-Strub TP, Batchelder HP, Spitz YH (2016) Characterizing the circulation off the Kenyan-Tanzanian coast using an ocean model. Journal of Geophysical Researchs 121: 1377-1399 [doi:10.1002/2015JC010860]

Ministry of Agriculture Livestock and Fisheries (2016) The Tanzanian fisheries sector: Challenges and opportunities. Technical report, Ministry of Agriculture Livestock and Fisheries, 40 pp

Nyandwi N (2013) The effects of monsoons on the East African Coastal Current through the Zanzibar Channel, Tanzania. Journal of Ocean Technology 8 (4): 65-74

Penven P, Marchesiello P, Debreu L, Lefe`vre J (2008) Software tools for pre- and post-processing of oceanic regional simulations. Environmental Modelling and Software 23: 660-662 [doi: 10.1016/j.envsoft.2007.07.004]

Peter JSF (2002) NPZ models of plankton dynamics: Their construction, coupling to physics, and application. Journal of Oceanography Review 58: 379-387

Ramanantsoa JD, Krug M, Penven P, Rouault M, Gula J (2018) Coastal upwelling south of Madagascar: Temporal and spatial variability. Journal of Marine Systems 178: 29–37 [doi: 10.1016/jmarsys.2017.10.005]

Ridgway KR, Dunn JR, Wilkin JL (2002) Ocean interpolation by four-dimensional least squares - Application to the waters around Australia. Journal of Atmospheric and Oceanic Technology. 19: 1357-1375 [doi: 10.1175/15200426(2002)019]

Rio MH, Guinehut S, Larnicol G (2011) The new CNES-CLS09 global mean dynamic topography computed from the combination of GRACE data, altimetry and in-situ measurements. Journal of Geophysical Research 116: C07018 [doi: 10.1029/2010JC006505]

Rio M-H, Hernandez F (2004) A mean dynamic topography computed over the world ocean from altimetry, in situ measurements, and a geoid model. Journal of Geophysical Research 109: C12032

Risien C, Chelton DB (2008) A global climatology of surface wind and wind stress fields from eight years of QuikSCAT Scatterometer data. Journal of Physical Oceanography 38: 2379-2413 [doi:10.1175/2008JPO3881.1]

Roberts MJ (2015) The western Indian Ocean upwelling research initiative (WIOURI): A flagship IIOE2 project. Clivar Exchange 68, 19 (3): 26-30

Roxy M, Ritika, K, Terray P, Masson S (2014) The curious case of Indian Ocean warming. Journal of Climatology 9: 8501-8509

Schott FA, Fieux M, Kindle J, Swallow J, Zantopp R (1988) The boundary currents east and north of Madagascar: 2 Direct measurements and model comparisons. Journal of Geophysical Research 93: 4963-4974

Schott FA, Shang-Ping X, McCreary JP (2009) Indian Ocean climate variability. Reviews of Geophysics 47: RG1002 (1–46) [doi: 10.1029/2007RG000245]

Shchepetkin AF, McWilliams JC (2005) The regional oceanic modeling system (ROMS): a split- explicit, free-surface, topography-following-coordinate oceanic model. Ocean Modelling 9: 347-404 [doi:10.1016/j.ocemod.2004.08.002]

Smith-Boughner L, Constable C (2012) Spectral estimation for geophysical time-series with inconvenient gaps. Geophysical Journal International 190: 1404-1422 [doi:10.1111/J.1365-246X.2012. 05594.X]

Swallow J, Schott FA, Fieux M (1991) Structure and transport of the East African Coastal Current. Journal of Geophysical Research 93: 4951-4962

Thomson D.J (1982) Spectrum estimation and harmonic analysis, Proceedings. Institute of Electrical Electronics Engineers 70, 1055-1096